

**Theoretical analysis of the inverse Edelstein effect at the LaAlO_3 / SrTiO_3 interface
with an effective tight-binding model: Important role of the second d_{xy} subband**

Shoma Arai¹, Shingo Kaneta-Takada¹, Le Duc Anh^{1,2}, Masaaki Tanaka^{1,3}, and Shinobu Ohya^{1,2,3*}

¹*Department of Electrical Engineering and Information Systems, The University of Tokyo, Hongo, Bunkyo-ku, Tokyo 113-8656, Japan*

²*Institute of Engineering Innovation, Graduate School of Engineering, The University of Tokyo, Bunkyo-ku, Tokyo 113-8656, Japan*

³*Center for Spintronics Research Network, Graduate School of Engineering, The University of Tokyo, Hongo, Tokyo 113-8656, Japan*

*E-mail: ohya@cryst.t.u-tokyo.ac.jp

The two-dimensional electron gas formed at interfaces between SrTiO_3 and other materials has attracted much attention since extremely efficient spin-to-charge current conversion has been recently observed at these interfaces. This has been attributed to their complicated quantized multi-orbital structures with a topological feature. However, there are few reports quantitatively comparing the conversion efficiency values between experiments and theoretical calculations at these interfaces. In this study, we theoretically explain the experimental temperature dependence of the spin-to-charge current conversion efficiency using an 8×8 effective tight-binding model considering the second d_{xy} subband, revealing the vital role of the quantization of the multi-band structure.

In spintronics, developing material systems enabling highly efficient spin-charge conversion is strongly demanded for exploring low-power-consumption non-volatile devices, such as spin-orbit-torque magnetoresistive random access memory.¹⁾ The two-dimensional electron gas (2DEG) formed at the SrTiO₃ (STO) interface, such as LaAlO₃ (LAO)/STO, is very promising because of its large Rashba spin-orbit interaction (SOI).^{2,3)} SOI causes spin splitting of the Fermi surface into the ones with different spin chirality, causing the spin-charge conversion in the 2DEG region [Fig. 1(a)]. The spin-to-charge conversion at material interfaces is called the inverse Edelstein effect (IEE),⁴⁻⁸⁾ and its conversion efficiency j_c^{2D}/j_s is called the inverse Edelstein length λ_{IEE} , where j_s is the injected spin current density and j_c^{2D} is the generated two-dimensional current density in the 2DEG region. At the STO interface, previous studies have demonstrated significantly large λ_{IEE} values up to ~ 60 nm,⁹⁻¹⁵⁾ which are thought to originate from its characteristic band structure: As shown in recent angle-resolved photoemission spectroscopy (ARPES) measurements, d -electrons are quantized due to band bending induced by the electric field near the interface in STO,¹⁶⁾ generating a complicated multi subband structure with a topological feature.¹⁷⁾ In particular, the second d_{xy} subband seems to contribute to the IEE substantially.¹⁸⁾ However, there are few reports quantitatively comparing the λ_{IEE} values between experiments and theoretical calculations based on the observed subband structure. Vaz *et al.* reported the experimental gate-voltage dependence of the λ_{IEE} using the 2DEG formed at AlO_x/STO and compared it with a calculation result.¹⁵⁾ They calculated the Edelstein-effect efficiency using a semiclassical Boltzmann transport theory and a tight-binding model, which characterize the spin density as a response to an externally applied electric field.^{15,17,19)} Meanwhile, the effective tight-binding model proposed by Kim *et al.*²⁰⁾ is convenient for calculating the λ_{IEE} , because the way to solve

the eigen equations derived from this model has been well studied and established.²¹⁾ In this study, we calculate the λ_{IEE} considering the second d_{xy} subband using the effective tight-binding calculation^{15,18,22)} and compare the calculated result with previous experimental data obtained for the 2DEG at the LAO/STO interface [Fig. 1(b)].²³⁾ The experimental temperature dependence of the λ_{IEE} is well reproduced by our theoretical calculation considering the second d_{xy} subband with reasonable physical parameters. We find that the second d_{xy} subband has a substantial contribution to the λ_{IEE} in this material system.

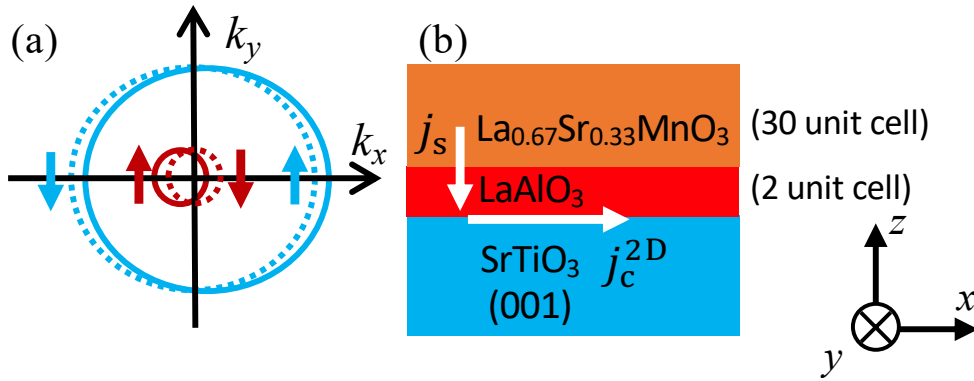


Fig. 1. (Color online) (a) Mechanism of the spin-to-charge current conversion via the inverse Edelstein effect in a simple parabolic-band picture. The spin current injected into the 2DEG region at the LAO/STO interface moves the outer and inner Fermi circles in opposite directions, generating a charge current in the x direction. Here, the dotted and solid lines are the Fermi circles before and after the spin current is injected, respectively. (b) All-epitaxial oxide heterostructure used for the spin-to-charge current conversion experiment in our previous study.²³⁾ The spin current is injected from ferromagnetic $\text{La}_{0.67}\text{Sr}_{0.33}\text{MnO}_3$ (LaSrMnO_3) and converted to the charge current in the 2DEG region at the LAO/STO interface.

For the band calculation, we use the 8×8 Hamiltonian, for which we extend the 6×6 model proposed by Kim *et al.* by adding a basis of the second d_{xy} subband.²⁰⁾ As shown

in previous ARPES measurements, the second d_{xy} subband is observed just below the Fermi level E_F due to its relatively weak quantization, while the second and higher subbands of d_{yz} and d_{zx} do not appear below E_F due to strong quantization.¹⁵⁾ In the following, H_0 expresses onsite interaction (diagonal in orbital space) and nearest-neighbor hopping; H_{ASO} represents spin-orbit interaction of atoms; H_a represents nearest-neighbor hopping induced primarily by polar lattice distortion due to the electric field originating from broken inversion symmetry. Using the eight t_{2g} orbitals of STO, $d_{yz}\uparrow$, $d_{yz}\downarrow$, $d_{zx}\uparrow$, $d_{zx}\downarrow$, $d_{xy}1\uparrow$, $d_{xy}1\downarrow$, $d_{xy}2\uparrow$, and $d_{xy}2\downarrow$ as basis functions, H_0 , H_{ASO} , and H_a are written as

$$H_0 = \begin{pmatrix} \frac{\hbar^2 k_x^2}{2m_h} + \frac{\hbar^2 k_y^2}{2m_l} & 0 & 0 & 0 \\ 0 & \frac{\hbar^2 k_x^2}{2m_l} + \frac{\hbar^2 k_y^2}{2m_h} & 0 & 0 \\ 0 & 0 & \frac{\hbar^2 k_x^2}{2m_l} + \frac{\hbar^2 k_y^2}{2m_l} - \Delta_{\text{E1}} & 0 \\ 0 & 0 & 0 & \frac{\hbar^2 k_x^2}{2m_l} + \frac{\hbar^2 k_y^2}{2m_l} - \Delta_{\text{E2}} \end{pmatrix} \otimes \sigma_0, \quad (1)$$

$$H_{\text{ASO}} = \Delta_{\text{ASO}} \begin{pmatrix} 0 & i\sigma_z & -i\sigma_y & -i\sigma_y \\ -i\sigma_z & 0 & i\sigma_x & i\sigma_x \\ i\sigma_y & -i\sigma_x & 0 & 0 \\ i\sigma_y & -i\sigma_y & 0 & 0 \end{pmatrix}, \quad (2)$$

$$H_a = \Delta_z \begin{pmatrix} 0 & 0 & ik_x & ik_x \\ 0 & 0 & ik_y & ik_y \\ -ik_x & -ik_y & 0 & 0 \\ -ik_x & -ik_y & 0 & 0 \end{pmatrix} \otimes \sigma_0, \quad (3)$$

where \hbar is the Dirac constant, k_x and k_y are the wavenumbers in the x and y directions, respectively, Δ_{E1} (Δ_{E2}) represents the energy difference at the Γ point ($k_x = k_y = 0$) between the first (second) d_{xy} subband and the d_{yz} band, which is lifted from the first d_{xy} subband bottom due to the confinement of the wave function in the z direction. Δ_{ASO} and Δ_z represent the magnitudes of H_{ASO} and H_a , respectively. σ_0 is the identity matrix in spin

space, and σ_x , σ_y , and σ_z are the spin matrices. \otimes is the Kronecker product. m_l ($= 0.41 m_0$) and m_h ($= 6.8 m_0$) are the effective masses of the light and heavy electrons at the LAO/STO interface, respectively, and m_0 is the free electron mass.²⁴⁾ To check the influence of the second d_{xy} subband on the λ_{IEE} , we also carry out the calculation using the 6×6 model without considering the basis of the second d_{xy} subband. Figure 2 shows the band structure obtained from the Hamiltonian $H = H_0 + H_{ASO} + H_a$ when both Δ_{ASO} and Δ_z are set at 10 meV. Here, a represents the lattice constant of STO. One can see that the red curve originating from the second d_{xy} subband is added in Fig. 2(b) in comparison with the result obtained with the 6×6 model [Fig. 2(a)]. As shown in the enlarged view of the band structure in the inset of Fig. 2(b), we can see that each band is spin-split due to SOI.

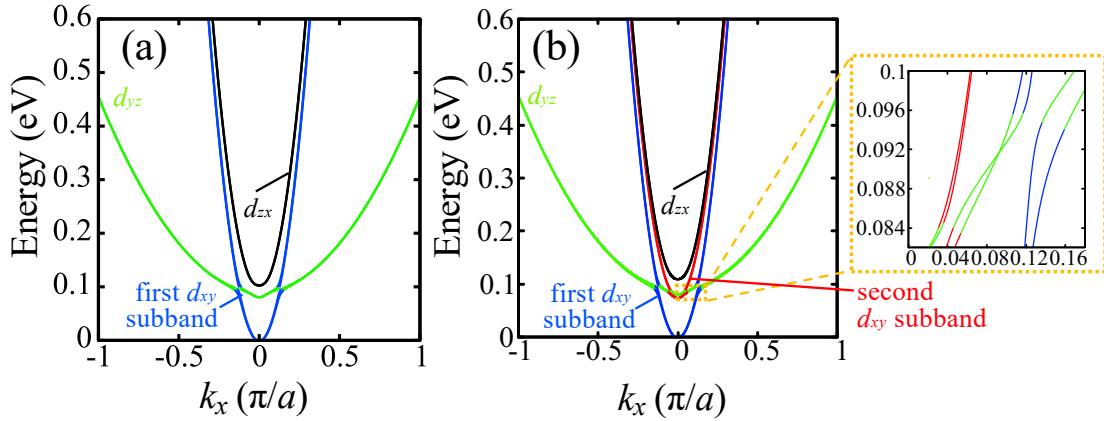


Fig. 2. (Color online) (a) Band structure obtained without considering the second d_{xy} subband (6×6 model). (b) Band structure obtained with the second d_{xy} subband (8×8 model). The black curve represents the d_{zx} band, the red curve represents the second d_{xy} subband, the blue curve is the first d_{xy} subband, and the green curve is the d_{yz} band. Here, $\Delta_z = 10$ meV, $\Delta_{ASO} = 10$ meV, $\Delta_{E1} = 0.09$ eV, and $\Delta_{E2} = 0.01$ eV. The enlarged image shows the band structure near the band crossing point.

We calculate the λ_{IEE} using the energy dispersion and the eigenstate derived from H at each \mathbf{k} [= (k_x, k_y)] point with fixed energy. Using the Boltzmann equation, j_c^{2D} and j_s are derived by the following equations:²⁵⁾

$$j_c^{\text{FS}n} = \frac{e^2}{4\pi^2\hbar} \int^{\text{FS}n} F_x(\mathbf{k}) dS_F, \quad (4)$$

$$\delta S^{\text{FS}n} = \frac{e}{4\pi^2\hbar} \int^{\text{FS}n} |S_y(\mathbf{k})| dS_F, \quad (5)$$

$$j_c^{2D} = \sum_n j_c^{\text{FS}n}, \quad (6)$$

$$j_s = \sum_n \frac{e \delta S^{\text{FS}n}}{\tau}, \quad (7)$$

where $F_x(\mathbf{k})$ and $S_y(\mathbf{k})$ are defined as follows:

$$F_x(\mathbf{k}) = F \operatorname{sgn}(S_y(\mathbf{k})) \tau(|\mathbf{k}|) v_x(\mathbf{k}) \frac{v_x(\mathbf{k})}{|\mathbf{v}(\mathbf{k})|}, \quad (8)$$

$$S_y(\mathbf{k}) = F \tau(|\mathbf{k}|) \sigma_y(\mathbf{k}) \frac{v_x(\mathbf{k})}{|\mathbf{v}(\mathbf{k})|}. \quad (9)$$

Here, F is the electric field generated in the 2DEG region, e is the electron charge, $\delta S^{\text{FS}n}$ is the spin accumulation, $\tau(|\mathbf{k}|)$ is the momentum relaxation time of the electron at each \mathbf{k} point, $\mathbf{v}(\mathbf{k}) = (v_x(\mathbf{k}), v_y(\mathbf{k}))$ is the group velocity, $\sigma_y(\mathbf{k})$ is the spin magnitude in the y direction, and dS_F is the infinitesimal area (= length in two dimensions) of the Fermi surface. In Eqs. (4) and (5), we conduct the integration over the n th Fermi surface $\text{FS}n$. From Eqs. (4), (6), and (8), the relationship between j_c^{2D} and F is expressed as

$$j_c^{2D} = \sum_n \frac{e^2}{4\pi^2\hbar} \int^{\text{FS}n} F \tau(|\mathbf{k}|) v_x(\mathbf{k}) \frac{v_x(\mathbf{k})}{|\mathbf{v}(\mathbf{k})|} dS_F. \quad (10)$$

We define the averaged momentum relaxation time τ as

$$\tau = \left[\sum_n \int^{\text{FS}n} \tau(|\mathbf{k}|) dS_F \right] / \left(\sum_n \int^{\text{FS}n} dS_F \right). \quad (11)$$

Here, $\tau(|\mathbf{k}|)$ is assumed to be proportional to $|\mathbf{k}|$. Then, the value of τ is estimated from Eq. (10) with derived $\mathbf{v}(\mathbf{k})$ and the experimental sheet resistance ($= F / j_c^{2D}$).

Figure 3 shows the calculated Fermi surface plotted with $v_x(\mathbf{k})$ and the spin direction $\langle \boldsymbol{\sigma} \rangle$ at $E_F = 140$ meV (measured from the first d_{xy} subband bottom), where $\boldsymbol{\sigma}$ is defined as $(\sigma_x, \sigma_y, \sigma_z)$. Using the eigenvector $\mathbf{C}_{\mathbf{k}}$ obtained at each \mathbf{k} point, $\langle \boldsymbol{\sigma} \rangle$ is expressed as $\mathbf{C}_{\mathbf{k}}^\dagger \boldsymbol{\sigma} \mathbf{C}_{\mathbf{k}}$. Along the k_x axis at $k_y = 0$, the Fermi surfaces from the outside correspond to the d_{yz} band, first d_{xy} subband, second d_{xy} subband, and d_{zx} band. As shown in Fig. 3(a), at around $k_y = 0$, the second d_{xy} subband has the next largest v_x after the first d_{xy} subband. As explained later, this result suggests that the second d_{xy} subband largely contributes to the IEE. Although each band splits into the outer and inner Fermi surfaces, this split is small and is not distinguishable on this scale. Thus, we plot the spin split outer and inner Fermi surfaces of each band separately in the left and right side of Fig. 3(b), respectively. In both figures, at $k_y = 0$, starting from the outer Fermi surface, the spin directions are $|\uparrow\rangle$, $|\downarrow\rangle$, $|\downarrow\rangle$, and $|\uparrow\rangle$. This order agrees with a previous result obtained by a density functional theory calculation.²⁶⁾

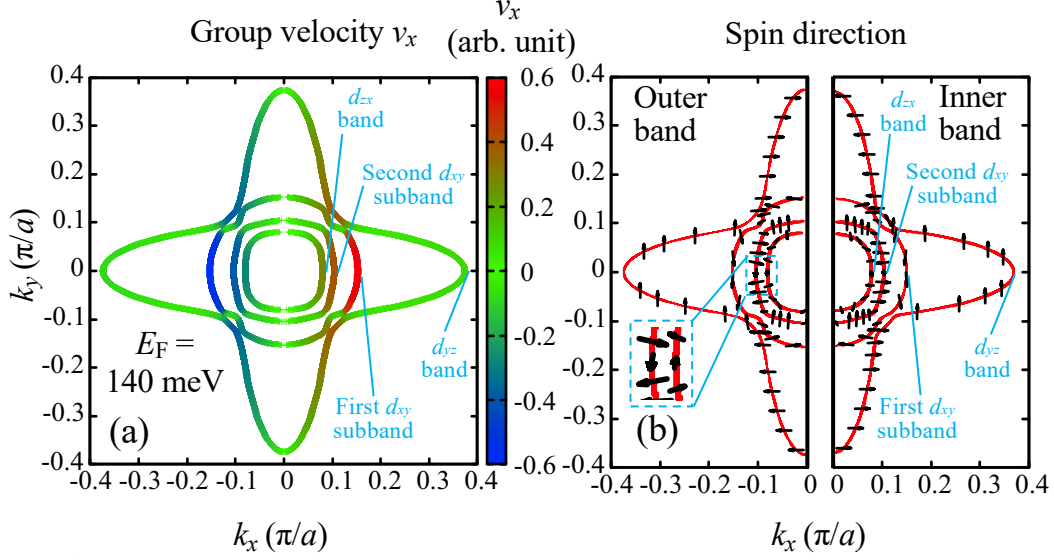


Fig. 3. (Color online) (a) Fermi surface mapped with the group velocity v_x in the x direction at $E_F = 140$ meV. (b) Fermi surface mapped with the spin direction at each \mathbf{k} point at $E_F = 140$ meV. In (b), the left (right) side shows only the outer (inner) band. Here, the Fermi surface at $E_F = 140$ meV is shown as an example because one can easily understand that band crossing generates the complicated Fermi surface near this energy.

Figure 4 shows the E_F dependence of $j_c^{2D}/\delta s [= (\tau / e) \times (j_c^{2D}/j_s)$, see Eqs. (6) and (7)] derived when the second d_{xy} subband is taken into account (red) and when it is not taken into account (blue). Here, δs is the summation of $\delta s^{\text{FS}n}$ over all n . One can see that $j_c^{2D}/\delta s$ increases by incorporating the second d_{xy} subband when E_F is above ~ 0.95 eV, at which the band bottom of the second d_{xy} band is located. Because j_c^{2D} is obtained by integrating $F_x(\mathbf{k})$ as shown in Eqs. (4) and (6), and because $F_x(\mathbf{k})$ is proportional to $v_x(\mathbf{k})$ as shown in Eq. (8), the charge current converted from the spin current is mainly composed of electrons with large $v_x(\mathbf{k})$. Thus, from Fig. 3(a), one can see that the first and second d_{xy} subbands have the main contribution to the λ_{IEE} . This is the most probable reason for the increase in the λ_{IEE} by considering the second d_{xy} subband.

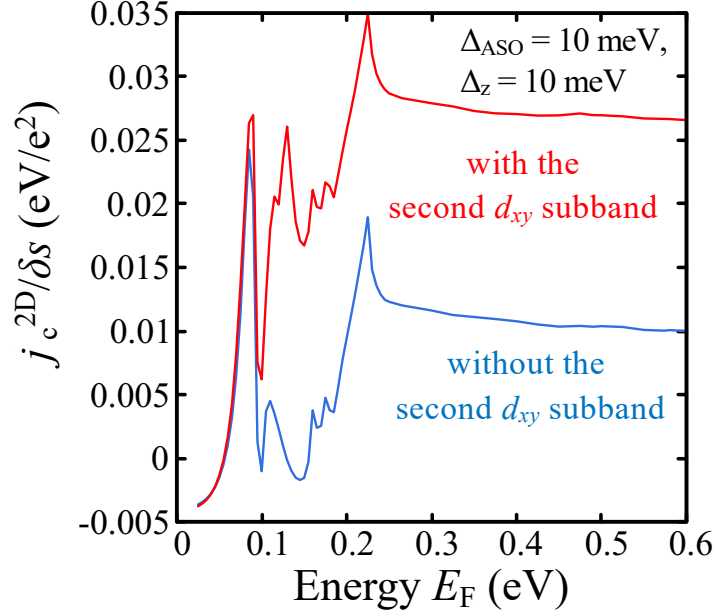


Fig. 4. (Color online) E_F dependence of $j_c^{2D}/\delta s$ when the second d_{xy} subband is taken into account (red line) when it is not (blue line).

In the following, we compare the experimental temperature dependence and calculation results of the λ_{IEE} using the 8×8 model. Here, we approximate that the IEE occurs only at the E_F because the signals were mainly obtained at low temperatures less than 150 K in the experiment.²³⁾ We determine the E_F value at each temperature so that the carrier density n calculated by the Green function method using the band dispersion shown in Fig. 2(b)²⁷⁾ equals the experimental one; $(E_F, n) = (210 \text{ meV}, 2.13 \times 10^{14} \text{ cm}^{-2})$, $(220 \text{ meV}, 2.21 \times 10^{14} \text{ cm}^{-2})$, $(265 \text{ meV}, 2.90 \times 10^{14} \text{ cm}^{-2})$, $(375 \text{ meV}, 4.64 \times 10^{14} \text{ cm}^{-2})$, $(490 \text{ meV}, 6.39 \times 10^{14} \text{ cm}^{-2})$, and $(580 \text{ meV}, 7.43 \times 10^{14} \text{ cm}^{-2})$ at 20, 40, 60, 80, 100, and 140 K, respectively.

Figure 5 shows the comparison between the theoretical and experimental results of the λ_{IEE} as a function of temperature. The calculated results show good agreement with the experimental results for $\Delta_{ASO} = 20 \text{ meV}$ when the second d_{xy} subband is not considered

and for $\Delta_{\text{ASO}} = 10$ meV when the second d_{xy} subband is considered. Here, we discuss the value of the effective Rashba coefficient $\alpha_{\text{eff}} = \hbar^2 \Delta k / (2m)$, where we define Δk as maximum band spin-splitting in the k_x direction at $k_y = 0$ for the first d_{xy} subband (*i.e.* $E_F = 85$ meV). When $\Delta_z = 10$ meV and $\Delta_{\text{ASO}} = 10$ meV, α_{eff} is estimated to be 8.15×10^{-13} eVm when we incorporate the second d_{xy} subband, which almost agrees with the reported values of α_{eff} ($\sim 1.2 \times 10^{-12}$ eVm) for LAO/STO.³⁾ For comparison, we calculate α_{eff} using the 6×6 model. α_{eff} is estimated to be 1.48×10^{-12} eVm, which is larger than that obtained with the 8×8 model. Both 6×6 and 8×8 models can reproduce the temperature dependence of the λ_{IEE} ; however, since the second d_{xy} subband is observed by ARPES measurements,¹⁵⁾ we need to incorporate the second d_{xy} subband.

Our results show that the experimental results of the temperature dependence of the λ_{IEE} can be well explained by our theoretical calculation considering the second d_{xy} subband with reasonable physical parameters. As shown in Fig. 4, this calculation indicates that the quantization of the d_{xy} band has a significant influence on the spin-to-charge conversion, suggesting that we can enhance the conversion efficiency by controlling the quantization of interfacial bands with the same spin chirality. In particular, controlling the quantum confinement for each band will be vital for such multiband materials like STO. Moreover, in Fig. 3 (b), one can see characteristic topologically non-trivial avoided anti-crossing points between the second d_{xy} subband and d_{yz} band at around $(k_x, k_y) = (\pm 0.085 \pi/a, \pm 0.085 \pi/a)$, where the spin expectation value almost vanishes (the length of the spin arrows becomes nearly zero). This characteristic feature can be attributed to the large spin-orbit interaction of this system.¹⁵⁾ Because the electron states near these points have finite $v_x(\mathbf{k})$, they largely contribute to the λ_{IEE} , which suggests the

importance of quantization in systems with large SOI. Our findings will help develop and design material interfaces with large spin-charge conversion in the future.

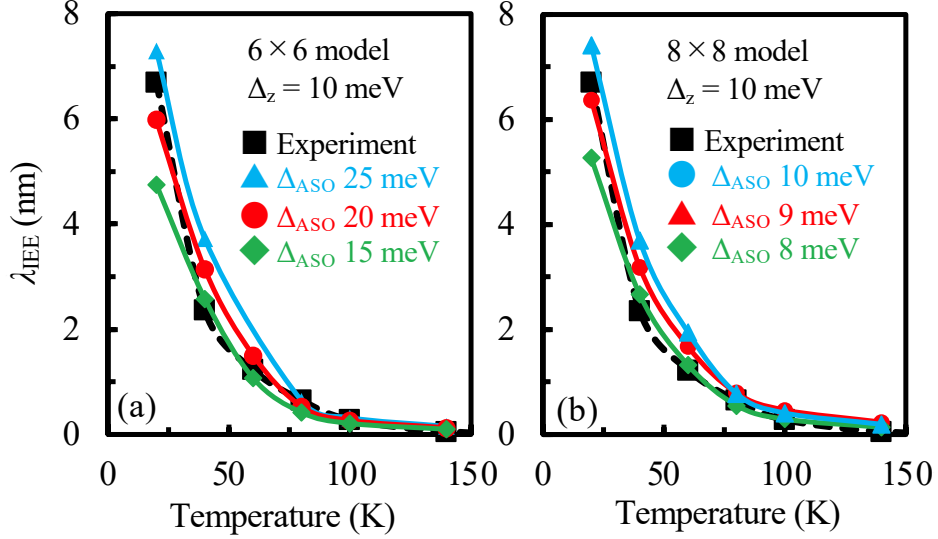


Fig. 5. (Color online) (a) and (b) Temperature dependence of the experimental (black)²³⁾ and calculated λ_{IEE} values (blue, red, and green curves). The calculated λ_{IEE} values in (a) represent the results obtained without considering the second d_{xy} subband (6x6 model). The ones in (b) represent the results obtained when considering the second d_{xy} subband (8x8 model).

In summary, to explain the temperature dependence of the λ_{IEE} obtained at the LAO/STO interface, we have performed a theoretical calculation incorporating the second d_{xy} subband using an effective tight-binding model. The calculation result considering the second d_{xy} subband reproduces the experimental results well with the reasonable parameters. We have found that the second d_{xy} subband has a large contribution to the λ_{IEE} . Our study gives us a clue to search for materials that exhibit highly efficient spin-charge conversion and will lead to a deeper understanding of this phenomenon.

ACKNOWLEDGEMENTS

This work was partly supported by Grants-in Aid Scientific Research (18H03860), the CREST program of Japan Science and Technology Agency (JPMJCR1777), and Spintronics Research Network of Japan.

REFERENCES

1. F. Oboril, R. Bishnoi, M. Ebrahimi, and M. B. Tahoori, IEEE Trans. Comput.-Aided Design Integr. Circuits Syst. **34**, 367 (2015).
2. A. Ohtomo and H. Y. Hwang, Nature **427**, 423 (2004).
3. A. D. Caviglia, M. Gabay, S. Gariglio, N. Reyren, C. Cancellieri, and J.-M. Triscone, Phys. Rev. Lett. **104**, 126803 (2010).
4. J. C. Rojas-Sánchez, L. Vila, G. Desfonds S. Gambarelli, J. P. Attané, J. M. De Teresa, and A. Fert, Nat. Commun. **4**, 2944 (2013).
5. P. Noel, C. Thomas, Y. Fu, L. Vila, B. Haas, P-H. Jouneau, S. Gambarelli, T. Meunier, P. Ballet, and J. P. Attané, Phys. Rev. Lett. **120**, 167201 (2018).
6. S. Oyarzún, A. K. Nandy, F. Rortais, J. C. Rojas-Sánchez, M. T. Dau, P. Noël, and M. Jamet, Nat. Commun. **7**, 13857 (2016).
7. J.-C. Rojas-Sánchez, S. Oyarzún, Y. Fu, A. Marty, C. Vergnaud, S. Gambarelli, L. Vila, M. Jamet, Y. Ohtsubo, A. Taleb-Ibrahimi, P. Le Fèvre, F. Bertran, N. Reyren, J.-M. George, and A. Fert, Phys. Rev. Lett. **116**, 096602 (2016).
8. J.-C. Rojas-Sánchez and A. Fert, Phys. Rev. Appl. **11**, 054049 (2019).
9. E. Lesne, Y. Fu, S. Oyarzun, J. C. Rojas-Sánchez, D. C. Vaz, H. Naganuma, G.

- Sicoli, J. P. Attané, M. Jamet, E. Jacquet, J. M. George, A. Barthélémy, H. Jaffrès, A. Fert, M. Bibes, and L. Vila, *Nat. Mater.* **15**, 1261 (2016).
10. Q. Song, H. Zhang, T. Su, W. Yuan, Y. Chen, W. Xing, J. Shi, J. Sun, and W. Han, *Sci. Adv.* **3**, e1602312 (2017).
 11. Y. Wang, R. Ramaswamy, M. Motapothula, K. Narayanapillai, D. Zhu, J. Yu, T. Venkatesan, and H. Yang, *Nano Lett.* **17**, 7659 (2017).
 12. J. Y. Chauleau, M. Boselli, S. Gariglio, R. Weil, G. De Loubens, J. M. Triscone, and M. Viret, *Europhys. Lett.* **116**, 17006 (2016).
 13. W. Zhang, Q. Wang, B. Peng, H. Zeng, W. T. Soh, C. K. Ong, and W. Zhang, *Appl. Phys. Lett.* **109** 262402 (2016).
 14. P. Noël, F. Trier, L. M. V. Arche, J. Bréhin, D. C. Vaz, V. Garcia, S. Fusil, A. Barthélémy, L. Vila, M. Bibes and J. P. Attané, *Nature* **580**, 483 (2020).
 15. D. C. Vaz, P. Noël, A. Johansson, B. Göbel, F. Y. Bruno, G. Singh, S. M. K. Walker, F. Trier, L. M. V. Arche, A. Sander, S. Valencia, P. Bruneel, M. Vivek, M. Gabay, N. Bergeal, F. Baumberger, H. Okuno, A. Barthélémy, A. Fert, L. Vila, I. Mertig, J. P. Attané, and M. Bibes, *Nat. Mater.* **18**, 1187 (2019).
 16. A. F. Santander-Syro, O. Copie, T. Kondo, F. Fortuna, S. Pailhès, R. Weht, X. G. Qiu, F. Bertran, A. Nicolaou, A. Taleb-Ibrahimi, P. Le Fèvre, G. Herranz, M. Bibes, N. Reyren, Y. Apertet, P. Lecoeur, A. Barthélémy, and M. J. Rozenberg, *Nature* **469**, 189 (2011).
 17. M. Vivek, M. O. Goerbig, and M. Gabay, *Phys. Rev. B* **95**, 165117 (2017).
 18. P. Bruneel and M. Gabay, *Phys. Rev. B* **102**, 144407 (2020).
 19. K. Shen, G. Vignale, and R. Raimondi, *Phys. Rev. Lett.* **112**, 096601 (2014).
 20. Y. Kim, R. M. Lutchyn, and C. Nayak, *Phys. Rev. B* **87**, 245121 (2013).
 21. Y. X. Liu, D. Z. -Y. Ting, and T. C. McGill, *Phys. Rev. B* **54**, 5675 (1996).

- 22. A. Johansson, B. Göbel, J. Henk, M. Bibes, and I. Mertig, Phys. Rev. Res. **3**, 013275 (2021).
- 23. S. Ohya, D. Araki, L. D. Anh, S. Kaneta, M. Seki, H. Tabata, and M. Tanaka, Phys. Rev. Res. **2**, 012014(R) (2020).
- 24. Z. Zhong, A. Tóth, and K. Held, Phys. Rev. B **87**, 161102(R) (2013).
- 25. P. Gambardella and I. M. Miron, Philos. Trans, R. Soc., A **369**, 3175 (2011).
- 26. P. D. C. King, S. M. K. Walker, A. Tamai, A. De La Torre, T. Eknapakul, P. Buaphet, S. K. Mo, W. Meevasana, M. S. Bahramy, and F. Baumberger, Nat. Commun. **5**, 3414 (2014).
- 27. H. Bahlouli, A. D. Alhaidari, and M. S. Abdelmonem, Phys. Lett. A, **367**, 162 (2007).